Author Manuscript

Author Manuscript

Author Manuscript

Author Manuscript

HHS Public Access

Author manuscript

Mol Cell. Author manuscript; available in PMC 2022 January 07.

Published in final edited form as:

Mol Cell. 2021 January 07; 81(1): 38–48.e4. doi:10.1016/j.molcel.2020.10.039.

Structural Basis for High-Affinity Trapping of the $Na_V1.7$ Channel in its Resting State by Tarantula Toxin

Goragot Wisedchaisri[1,4], **Lige Tonggu**[1,4], **Tamer M. Gamal El-Din**[1], **Eedann McCord**[1,3], **Ning Zheng**[1,2,*], **William A. Catterall**[1,5,*]

[1]Department of Pharmacology, University of Washington, Seattle, WA, 98195, USA

[2]Howard Hughes Medical Institute, University of Washington, Seattle, WA, 98195, USA

[3]Present address: Department of Physiology and Biophysics, University of Washington, Seattle, WA, 98195, USA

[4]These authors contributed equally

[5]Lead contact

SUMMARY

Voltage-gated sodium channels initiate electrical signals and are frequently targeted by deadly gating-modifier neurotoxins, including tarantula toxins, which trap the voltage sensor in its resting state. The structural basis for tarantula-toxin action remains elusive, because of the difficulty of capturing the functionally relevant form of the toxin-channel complex. Here we engineered the model sodium channel Na_VAb with voltage-shifting mutations and the toxin-binding site of human $Na_V1.7$, an attractive pain target. This mutant chimera enabled us to determine the cryo-EM structure of the channel functionally arrested by tarantula toxin. Our structure reveals a high-affinity resting-state-specific toxin-channel interaction between a key lysine residue that serves as a ‘stinger’ and penetrates a triad of carboxyl groups in the S3-S4 linker of the voltage sensor. By unveiling this high-affinity binding mode, our studies establish a high-resolution channel-docking andresting-statelockingmechanism for huwentoxin-IV and provide guidance for developing future resting-state-targeted analgesic drugs.

eTOC Blurb

Wisedchaisri et al. report the cryo-EM structure of an engineered bacterial $Na_V1.7$ chimeric channel captured in the resting state by a tarantula toxin. They reveal how the toxin’s ‘stinger’

*Correspondence: nzheng@uw.edu and wcatt@uw.edu.

AUTHOR CONTRIBUTIONS

G.W., L.T., T.M.G., E.M., N.Z., and W.A.C. designed the experiments; G.W., L.T., T.M.G., and E.M. carried out the experiments; all authors analyzed and interpreted the results; G.W., N.Z., and W.A.C. wrote the paper; and all authors reviewed and revised the paper.

DECLARATION OF INTERESTS

The authors declare no competing interests.

Publisher's Disclaimer: This is a PDF file of an unedited manuscript that has been accepted for publication. As a service to our customers we are providing this early version of the manuscript. The manuscript will undergo copyediting, typesetting, and review of the resulting proof before it is published in its final form. Please note that during the production process errors may be discovered which could affect the content, and all legal disclaimers that apply to the journal pertain.

Author Manuscript Author Manuscript Author Manuscript Author Manuscript

immobilizes prey at the atomic level and suggest a way to design future resting-state-targeted analgesic drugs.

Graphical Abstract

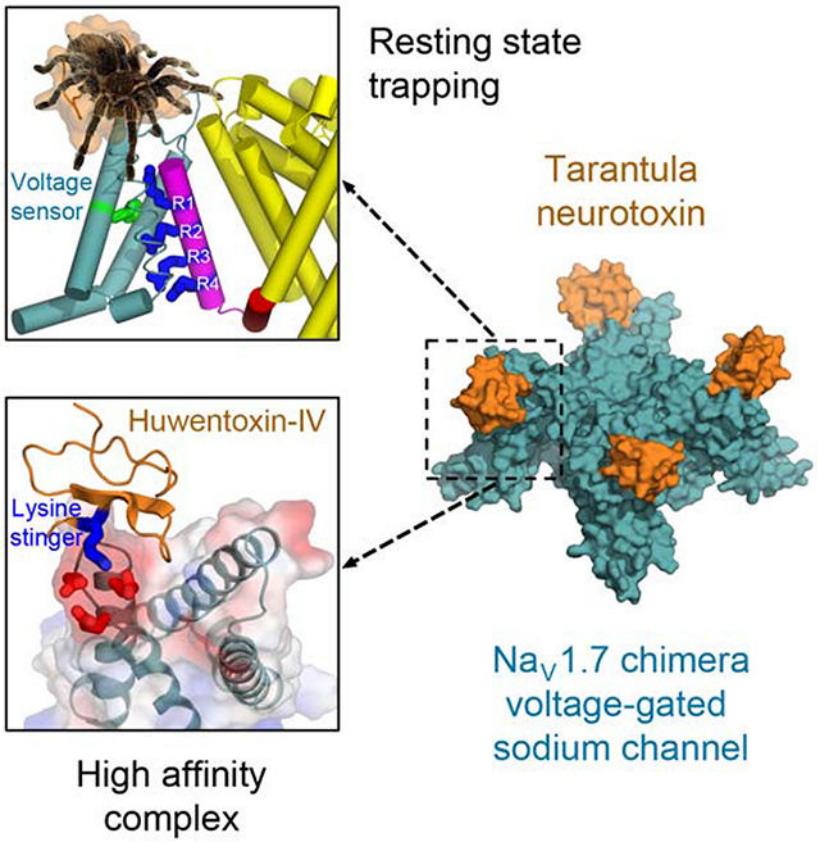

INTRODUCTION

Voltage-gated sodium channels (Na_V) generate and propagate action potentials in nerve and muscle (Hille, 2001; Hodgkin and Huxley, 1952), but the structural basis for their function and pharmacology remains incompletely defined. Upon membrane depolarization, Na_V channels transition from the resting state to the activated state, open a Na^+-selective transmembrane pore, and then inactivate within a few milliseconds (Hille, 2001; Hodgkin and Huxley, 1952). Na_V channels in eukaryotes are composed of a single large polypeptide with 24 transmembrane segments organized in four homologous domains (I-IV) (Catterall, 1984, 1986; Numa and Noda, 1986). Each homologous domain contains six transmembrane segments separated into two functional modules, the voltage-sensing module (VS, segments S1-S4) and the pore-forming module (PM, segments S5-P-S6) (Ahern et al., 2016; Catterall, 1986; Catterall et al., 2017). Each S4 segment contains four to eight repeated motifs of a positively charged amino acid residue (usually Arg) flanked by two hydrophobic residues (Ahern et al., 2016; Bezanilla, 2000; Catterall, 1986; Catterall et al., 2017). Changes in membrane potential exert an electrostatic force on these S4 gating charges, causing inward

Author Manuscript Author Manuscript Author Manuscript Author Manuscript

or outward movement of the S4 segment and coupling these transmembrane movements to conformational changes that open or close the pore (Ahern et al., 2016; Catterall, 1986; Catterall et al., 2017). Prokaryotic Na_V channels are simpler in structure, composed of four identical subunits that each is analogous to one domain of a eukaryotic Na_V channel (Payandeh et al., 2011; Ren et al., 2001). Thus, this fundamental mechanism of voltage sensing and pore opening is responsible for electrical signaling throughout biology (Gamal El-Din et al., 2018).

The molecular basis for Na_V channel function is being progressively elucidated by structural studies of prokaryotic and eukaryotic Na_V channels. Many structures of Na_V channels with their VS in activated or partially activated conformations have been determined at high resolution, beginning with the bacterial Na_V channel Na_VAb (Payandeh et al., 2011), and continuing with other bacterial (Shaya et al., 2014; Sula et al., 2017; Zhang et al., 2012b), and mammalian Na_V channels (Jiang et al., 2020; Pan et al., 2019; Pan et al., 2018; Shen et al., 2019). In contrast, structural studies of the resting state of Na_V channels have been more challenging because the resting state is only present at the negative resting membrane potential of −80 mV in nerve and muscle or −160 mV in bacteria. The structure of the resting state of Na_VAb was determined by stabilizing it at 0 mV with a combination of voltage-shifting mutations and disulfide locking (Wisedchaisri et al., 2019). This structure revealed key features of the resting state of the VS and supported a ‘sliding-helix’ mechanism of gating.

Neurotoxins from venomous animals target Na_V channels at multiple neurotoxin receptor sites in order to paralyze prey (Catterall, 1980; Hille, 1975, 2001; Lazdunski et al., 1986; Ritchie, 1979; Rochat et al., 1979). Gating-modifier toxins produce their dramatic physiological effects by voltage-sensor trapping; that is, by trapping the VS in either the resting or activated state by binding to it specifically with high affinity (Cestèle et al., 1998; Rogers et al., 1996; Sokolov et al., 2008; Xiao et al., 2008a; Zhang et al., 2012a). Polypeptide toxins from spiders and scorpions target neurotoxin receptor site 4 in domain II of Na_V channels and either prevent or inappropriately enhance activation of the VS (Catterall et al., 2007; Cestèle et al., 1998; Couraud et al., 1982; Schmalhofer et al., 2008; Sokolov et al., 2008; Xiao et al., 2008a; Xiao et al., 2014; Zhang et al., 2011, 2012a). Huwentoxin-IV (μ-theraphotoxin-Hs2a; HwTx-IV) from the Chinese bird tarantula *Haplopelma schmidti* (Peng et al., 2002; Xiao et al., 2008b) and Protoxin-II (β/ω-theraphotoxin-Tp2a; ProTx-II) from the Peruvian green velvet tarantula *Thrixopelma pruriens* (Middleton et al., 2002) inhibit human $Na_V1.7$ with nanomolar affinity. Structures of $Na_V1.7$ and its bacterial chimera constructs with ProTx-II and HwTx-IV bound to activated or partially activated conformations of the VS have been reported (Gao et al., 2020; Shen et al., 2019; Xu et al., 2019), although it has been suggested that the overall channel could be in the inactivated state (Shen et al., 2019). However, due to the long-standing challenges in isolating Na_V channels in their resting state, there is no structure of any inhibitory gating-modifier toxin bound in its high-affinity pose to the resting state of its channel target. The lack of such a structure leaves a major gap in our understanding of the molecular mechanism of action of these deadly toxins.

Author Manuscript Author Manuscript Author Manuscript Author Manuscript

In these studies, we imported the high-affinity binding site for HwTx-IV from the human neuronal $Na_V1.7$ channel into the ancestral Na_V channel Na_VAb, introduced voltage-shifting mutations to stabilize the toxin/channel complex in the resting state at 0 mV, and determined its structure at high resolution by cryo-EM. Our results reveal the structure of the resting state of an Na_V channel with a gating-modifier bound and define a high-resolution voltage sensor-trapping mechanism through which HwTx-IV opposes the electrostatic force generated by depolarizing stimuli and locks the $Na_V1.7$ in its resting state by inserting a 'stinger' Lys into the VS of its prey. Moreover, because $Na_V1.7$ is an actively investigated target for pain therapeutics, our results may offer guidance for future drug discovery efforts to develop much-sought first-in-class analgesic drugs that target the resting state of this key Na_V channel.

RESULTS

Design, construction, and characterization of a voltage-shifted $Na_VAb/Na_V1.7$-VS2 chimera

Chimeric channels in which portions of the VS of Na_VAb were replaced by corresponding segments of $Na_V1.7$ yielded a substantial positive shift in the voltage dependence of activation and sensitivity to modulation by the inhibitory gating-modifier toxin ProTx-II (Rajamani et al., 2017). We engineered Na_VAb to contain segments of the $Na_V1.7$ VS2 as a receptor site for HwTx-IV. We first aligned the VS sequences of $Na_V1.7$ VS2 and Na_VAb and then grafted $Na_V1.7$ VS2 nucleotide sequences encoding the S1-S2 and S3-S4 segments into corresponding segments of a cDNA encoding Na_VAb (Figures 1A–1C and S1). Several versions of the $Na_VAb/Na_V1.7$ VS2 chimera were constructed and characterized by electrophysiology (STAR Methods). The construct that yielded the largest positive shift in the voltage dependence of activation ($V_{1/2}$ = +34.6 ± 1.4 mV) was selected for this study (Figures 1D, 1E and S1). Subsequently, a voltage-shifting mutation previously used for stabilizing Na_VAb in the resting state (Wisedchaisri et al., 2019) was introduced into the chimera. This mutation (L834A in $Na_V1.7$) caused a further positive shift in the voltage dependence of activation to $V_{1/2}$ = +83.4 ± 0.9 mV (referred to as $Na_VAb/Na_V1.7$-VS2A; Figures 1D, 1E and S1). Most importantly, this chimera remains closed in the resting state at 0 mV at which our structural studies were conducted.

Functional voltage sensor trapping of a $Na_VAb/Na_V1.7$-VS2 chimera by an engineered HwTx-IV

The potent gating modifier toxin HwTx-IV has high affinity for $Na_V1.7$ (K_D = 26 nM; (Xiao et al., 2008a). Further peptide engineering of this toxin led to the discovery of m3-HwTx-IV with triple mutations of E1G, E4G, Y33W, which has improved affinity (K_D = 0.4 to 3.3 nM; (Rahnama et al., 2017; Revell et al., 2013)). We characterized the efficacy of m3-HwTx-IV for voltage-sensor trapping of our $Na_VAb/Na_V1.7$-VS2A chimera in its resting state. Perfusion of increasing concentrations of m3-HwTx-IV gave progressive reduction in the sodium current (Figure 2A). At 100 nM, the sodium current was nearly completely blocked at accessible membrane potentials (Figure 2B). The IC_{50} for the inhibition was 2.6 ± 0.13 nM for the chimera (Figure 2C), similar to values of 0.4 ± 0.1 nM and 3.3 ± 1.1 nM previously reported for intact human $Na_V1.7$ (Rahnama et al., 2017; Revell et al., 2013). Importantly, m3-HwTx-IV at 100 nM completely inhibited sodium current for the chimera

Author Manuscript Author Manuscript Author Manuscript Author Manuscript

(Figure 2B) until long, strong depolarizing pulses were applied (Figure 2D). The voltage-dependent reversal of voltage-sensor trapping was more rapid and complete upon depolarization to 160 mV, intermediate at 120 mV, and slower and incomplete in the time frame we studied at 80 mV (Figure 2D). These results show that the binding of m3-HwTx-IV inhibits the $Na_VAb/Na_V1.7$-VS2A chimeric channel by trapping it in the resting state and that this voltage-sensor trapping is reversed by a long, strong depolarization to expel the bound toxin, as observed previously for inhibitory gating-modifier toxins acting on eukaryotic sodium channels (Sokolov et al., 2008; Xiao et al., 2014).

Structure of $Na_VAb/Na_V1.7$-VS2A chimera with m3-HwTx-IV bound

Efforts to crystallize $Na_VAb/Na_V1.7$-VS2A with m3-HwTx-IV bound were unsuccessful. Therefore, we generated a fusion protein for cryo-EM imaging by linking the C-terminal alpha helix of maltose-binding protein (MBP)to the N-terminal alpha helix of $Na_VAb/Na_V1.7$-VS2A with a rigid Asn-Ala linker (Waugh, 2016). The MBP-$Na_VAb/Na_V1.7$-VS2A chimera and m3-HwTx-IV form a high-affinity complex that can be co-eluted during size-exclusion chromatography (Figure S2A), indicating a stable stoichiometric complex suitable for structural study. We assembled an MBP-$Na_VAb/Na_V1.7$-VS2A:m3-HwTx-IV complex at 1:8 molar ratio in GDN detergent, flash froze the sample on EM grids, and imaged the sample by cryo-EM using a Titan Krios system (Figures S2B and S2C; Methods). We reconstructed a 3D map to 3.6 Å overall resolution (Figure 3A), as assessed by the Fourier Shell Correlation (FSC) between independently refined half-maps with a criterion of 0.143 (Henderson et al., 2012) (Figure S2D). The density map has local resolution of ~3.5 Å in transmembrane segments of the VS and pore, and ~4–4.5 Å in the loops and S4-S5 linker (Figures 3A and S3A). The m3-HwTx-IV density is unambiguously present but the resolution ranges from ~4Å at the VS aqueous cleft to ~5 Å near detergent micelles (Figures 3A, S3B and S3C). Using the known structure of m3-HwTx-IV as a guide (Rahnama et al., 2017), we built an atomic model of the $Na_VAb/Na_V1.7$-VS2A:m3-HwTx-IV complex in the interpretable part of the map and refined the structure to give a high-resolution image of the toxin/channel complex (Figures 3B and S3).

Resting state conformation of $Na_V1.7$ VS2 with m3-HwTx-IV bound

Transmembrane helices S1-S4 of $Na_VAb/Na_V1.7$-VS2A adopt a canonical VS topology (Payandeh et al., 2011) in which the extracellular loops S1-S2 and S3-S4 form helical hairpins that create an aqueous cleft on the extracellular side (Figure 4A, left). Helix S4 adopts a 310 helical conformation, in which all four gating charge Arg's line up on one side of the helix with their side chains pointing toward helix S2 (Figure 4B, left). The S4 helix markedly assumes an "inward" conformation, in which the hydrophobic constriction site (HCS) residue F776 from S2 is wedged between the side chains of R1 and R2 such that R2-R4 are all on the intracellular side of the HCS. Gating charge R1 interacts with N769 from the ENC of S2, while R2 and R3 make ion-pair interactions with INC residues E779 from S2 and D801 from S3. R4 is located in the cytoplasm and stabilized by conserved W797 on the intracellular side of S3. As S4 partially dips into the cytoplasm in this "inward" conformation, an angle formed between S4 and the S4-S5 linker creates an elbow from which the S4-S5 linker rises toward the inner membrane surface to connect with the intracellular end of S5 and the pore (Figure 4C, left). Together, the S4-S5 linkers from all

Author Manuscript Author Manuscript Author Manuscript Author Manuscript

four subunits form a collar that wraps around S6 to hold the pore closed (Figure 4D, left, blue). The VS and S4-S5 linker conformations observed in the $Na_VAb/Na_V1.7$-VS2A:m3-HwTx-IV complex closely resemble the conformations identified previously in the disulfide-locked resting state structure of Na_VAb ((Wisedchaisri et al., 2019); RMSD = 0.98 Å over 125 Cα atoms for the S4 helix, S4-S5 linker, and the S5-S6 helices; Figure S4), indicating that m3-HwTx-IV traps VS2 in the same deep resting state in the absence of disulfide-locking.

Comparison of $Na_VAb/Na_V1.7$-VS2A trapped in the resting state by m3-HwTx-IV with $Na_V1.7$ VS2 in the activated state could reveal important insights into gating charge movement and mechanical coupling to the pore. Unfortunately, there is no available structure of $Na_V1.7$ apo-VS2 in the fully activated state. We therefore compare our structure with VS2 of human $Na_V1.7$ bound to HwTx-IV in a partially activated state (Shen et al., 2019) (Figure 4, right panels). This partially activated conformation of VS2 is consistent with an inactivated state of the $Na_V1.7$ channel as a whole, as suggested by Shen et al., because partial or full activation of the VS would be required to trigger inactivation. From the resting state of $Na_VAb/Na_V1.7$-VS2A, the S4 helix translocates outward by ~7.3 Å (~1.2 helical turns) toward the extracellular milieu to reach this partially activated “outward” conformation, which deepens the extracellular aqueous cleft (Figure 4A, right). This distance of movement is significantly less than the 11.5 Å translocation observed in the S4 segment of Na_VAb between resting and fully activated states, which corresponds to two complete helical turns (Wisedchaisri et al., 2019), suggesting that this state of the VS in human $Na_V1.7$ is only partially activated. Only side chains of gating charges R1 and R2 have moved outward completely through the HCS, but R3 is located at the same level as F776 in the HCS and R4 is completely on the intracellular side (Figure 4B, right). R1 and R2 interact with ENC while R4 interacts with INC. Evidently, binding of HwTx-IV by itself is not sufficient to move VS2 inward into its resting state at 0 mV without voltage-shifting mutations. Therefore, this complex of HwTx-IV with partially activated VS2 of $Na_V1.7$ is likely to be a low-affinity complex on the pathway to voltage-dependent toxin binding or dissociation (eg., Figure 2).

In the activated states of Na_VAb (Wisedchaisri et al., 2019) and both VS1 and VS3 of $Na_V1.7$ (Shen et al., 2019), gating charges R1-R3 fully translocate outward from the HCS. In contrast, the partial outward position of S4 in VS2 of the $Na_V1.7$ complex with HwTx-IV can likely be attributed to the association of HwTx-IV with this partially activated conformation of the S4 segment, which prevents VS2 from full activation. The outward movement of S4 also unbends the elbow and brings the S4-S5 linker from the cytoplasm to a position almost parallel to the membrane (Figure 4C, right), and in turn, loosens the collar around the S6 pore-lining helices as if they are poised to open the activation gate with further depolarization (Figure 4D, right).

Neurotoxin receptor site 4 with HwTx-IV bound in resting and partially activated states of the voltage sensor

In the resting state complex revealed by our results, m3-HwTx-IV interacts intimately with VS2 and penetrates into the aqueous cleft between the S1-S2 and the S3-S4 helical hairpins,

Author Manuscript Author Manuscript Author Manuscript Author Manuscript

as observed in a side view (Figure 5A). The penetration of the toxin between these two helical hairpins is seen in more detail in a top view (Figure 5A). These structural results are consistent with a high-affinity interaction between the toxin and its receptor site, which is illustrated in more detail in Figure 5C. m3-HwTx-IV inserts its Loop 4 and its conserved C-terminal "^{26}RK×RWCK^{32}" motif (Figure 6A, underlined) into the outer end of the VS2 aqueous cleft (Figure 5C). There are extensive interactions with amino acid residues in the S3-S4 loop. Negatively charged residues E811, D816, and E818 in the S3-S4 extracellular loop of VS2 interact with positively charged residues K27 and K32 of m3-HwTx-IV (Figure 5C). Remarkably, m3-HwTx-IV inserts K32 with its positively charged amino group like a "stinger" into this triad of negatively charged residues in its prey Figure 5C and S3C. The "^{812}LFLAD^{816}" motif (Figure 1C) in the S3-S4 loop of VS2 provides hydrophobic and van der Waals interactions with I5, F6, T28, W30, K32, and Q34 and nearby residues of m3-HwTx-IV with energy inversely proportional to the sixth power of their distance (Figure 5C). In contrast to these extensive interactions with the S3-S4 loop, residues E753 and N763 are the only residues in S1-S2 loop observed to interact directly with bound m3-HwTx-IV, through their close approach to K27 and R29, respectively (Figure 5C). F813, A815, D816 are unique to $Na_V1.7$ among Na_V subtypes (Figure 1C) and may be responsible for $Na_V1.7$ specificity.

Comparison with mutational studies reported previously for $Na_V1.7$ further illustrates the close binding interactions with amino acid residues whose mutation has large effects on toxin binding (Figures 6B and 6C). Mutation of residues colored in green to Ala gives an increase in affinity, whereas residues colored in shades of red give decreases in affinity from 2-fold to more than 20-fold as coded in the depth of color (Figure 6B). Mutations of E753Q, E811Q, L814A, D816A, and E818C each decreased HwTx-IV inhibition of NaV1.7 activation (Xiao et al., 2010). Double mutations of D816N/E818Q also greatly diminished HwTx-IV sensitivity for $Na_V1.7$ (Xiao et al., 2008a). On the toxin side, Ala substitutions of F6, W30, and K32 in HwTx-IV all decrease affinity for $Na_V1.7$ while Ala substitutions of I5 and T28 increase the affinity (Figures 6A and 6C) (Revell et al., 2013), which correlate well with our structural findings that these residues make contacts with $Na_V1.7$. Mutations of the 'stinger' K32 and its three negatively charged targets, E811, D816, and E818 have particularly strong effects (Figures 6B and 6C). Approximately 480 Å^2 of protein surface on each side of this interface interact to form the toxin/receptor complex. These intimately interacting binding surfaces revealed for m3-HwTx-IV and neurotoxin receptor site 4 support a specific high-affinity interaction.

In sharp contrast to this tight interaction of m3-HwTx-IV with VS2 in its resting state conformation, interactions of HwTx-IV with VS2 of $Na_V1.7$ in a partially activated state appear much less extensive in the structures presented by Shen et al (Figure 5B; (Shen et al., 2019)). Outward movement of the S4 segment in the partially activated state of the VS likely impedes tight binding of HwTx-IV to the S3-S4 loop, which is unresolved in this image (Figure 5B, side view; S4, purple; unresolved S3–S4 loop, yellow dashed line). Similarly, bound HwTx-IV does not penetrate into the cleft formed by the S3-S4 helical hairpins (Figure 5C, side view), perhaps because the presence of the S4 segment in an outward conformation would create a clash. The lack of clear molecular interactions between HwTx-IV and partially activated VS2, especially in the S3-S4 loop, is indicative of a low-affinity

Author Manuscript Author Manuscript Author Manuscript Author Manuscript

toxin-receptor complex. Consistent with this conclusion, we estimate that <300 $Å^2$ of protein surface contributes to this interface. The comparison of these two structures illustrates the essence of voltage-sensor trapping. Intimate, high-affinity interactions bind the toxin to neurotoxin receptor site 4 in the resting state and trap VS2 in that state. In contrast, voltage-driven outward movement of the S4 segment destabilizes the toxin-receptor complex by disrupting productive molecular interactions and changing the conformation of the S3-S4 helical hairpin in the partially activated state of VS2. These large differences in binding interactions produce the characteristic, strongly voltage-dependent unblock observed for gating modifier toxins (Figure 2; (Sokolov et al., 2008)). High-affinity binding of HwTx-IV to the resting state of VS2 is the structural basis for its deadly toxic effect, because only this high-affinity toxin/receptor complex can resist the electrostatic force of depolarization, trap the voltage sensor in its resting state, prevent channel activation, and paralyze prey.

DISCUSSION

HwTx-IV traps VS2 in the resting state

Our structure of m3-HwTx-IV bound to the $Na_VAb/Na_V1.7$-VS2A chimera in the resting state shows the tarantula toxin occupying the aqueous cleft of VS2 and interacting strongly with the S3-S4 loop to restrict S4 to an inward position projecting into the cytoplasm. This inward position reveals three gating charge Arg on the intracellular side of the HCS and implies exchange of ion-pair interactions from negatively charged residues in the ENC to those in the INC. This position of S4 creates an elbow connecting S4 to the S4-S5 linker, which points into the cytoplasm. The conformation observed here is nearly identical to the resting state conformation in the disulfide-locked resting state (Wisedchaisri et al., 2019), but it is captured here without any chemical modification. This structure verifies that (*i*) HwTx-IV traps the VS in the resting state to inhibit channel activation; (*ii*) the resting-state conformations of the VS and S4-S5 linker are likely universal in prokaryotic and eukaryotic Na_V channels; and (*iii*) the disulfide-locked resting state reported previously is not influenced by the disulfide crosslinking used to stabilize it. In this resting-state conformation of $Na_VAb/Na_V1.7$-VS2A, the S4 segment is like a cocked gun, ready to shoot out upon depolarization and initiate pore opening. The four S4-S5 linkers form a tight collar to restrict movement of the S6 segments that form the activation gate and keep the channel closed. This conformation reveals the fundamental structural mechanism of voltage-sensor trapping. The binding energy of m3-HwTx-IV imposes an inward resting position of the S4 segment and its gating charges and thereby inhibits voltage-dependent activation.

HwTx-IV binds deeper and with higher affinity in VS2 in the resting state

This structure of the high-affinity complex of m3-HwTx-IV with VS2 in the resting state stands in striking contrast to the previous structure of HwTx-IV bound to VS2 of $Na_V1.7$ in a partially activated state (Shen et al., 2019). In this previously reported structure, the S4 segment is in a partially activated position in VS2, with two gating charges completely outside the HCS, more than 7 Å outward from their resting state position. The S3-S4 loop is unresolved and may not be tightly bound to HwTx-IV in partially activated VS2 (Shen et al., 2019). HwTx-IV appears to make these superficial interactions because the outward position of S4 disrupts the structure of the S3-S4 helical hairpin and prevents access to deeper

Author Manuscript Author Manuscript Author Manuscript Author Manuscript

interaction sites. This comparison suggests that the high-affinity toxin-receptor complex forms only in the resting state, accompanied by unwinding the S3-S4 helical hairpin and deeper and tighter binding of HwTx-IV, which allows the 'stinger' Lys to penetrate the triad of negatively charged residues in the S3-S4 loop and lock the voltage sensor firmly in place. This mode of ligand interaction may be more widespread among ion channels, as a Lys residue is also observed to bind tightly in a cage of Trp residues in calmodulin complexes with TRP5 and TRP6 channels (Dang et al., 2019; Singh et al., 2018). Formation of this specific high-affinity complex with HwTx-IV effectively traps the voltage sensor in its resting state. Strong depolarization activates the VS, moves the S4 segment outward, and expels the bound toxin, perhaps through low-affinity intermediate states like the partially activated state of VS2 with HwTx-IV weakly bound (Figure 5; (Shen et al., 2019)). Thus, the essence of voltage-sensor trapping is revealed by the structure of m3-HwTx-IV bound to the resting state of VS2.

A two-step toxin-binding and voltage-sensor trapping mechanism

Our results suggest an unusual voltage-dependent two-step binding and voltage-sensor trapping mechanism, in which only the high-affinity resting state complex is productive in blocking channel activation. We speculate that HwTx-IV can bind loosely and with low affinity to VS2 through weak protein interactions with the S1-S2 and S3-S4 loops, even in a partially activated state of the VS. However, this binding interaction is not functionally significant because it occurs when the VS2 is already partially activated. In sharp contrast, a second step of high-affinity toxin interaction with the resting state is required for voltage-sensor trapping, which is the functionally important step in toxin action. As our structure shows, m3-HwTx-IV binds deeper in the aqueous cleft and forms a tight, high-affinity interaction with the S1-S2 and S3-S4 helical hairpins that thrusts a key positively charged 'stinger' Lys amino group into a triad of negative charges in its receptor site. Only this high-affinity toxin interaction covering 480 Å of protein surface on each side has sufficient stability to resist the force of the electrical field acting on the S4 gating charges and therefore is able to trap VS2 in its resting state and prevent sodium channel activation at physiological membrane potentials. We propose that the energy of this protein interaction is the deadly force through which the tarantula immobilizes its prey.

A common mode of action for NaSpTx toxins

Closely related toxins in the NaSpTx family 1 are likely to share a common mode of inhibition with HwTx-IV. Hainantoxin-IV (β-theraphotoxin-Hhn1b; HnTx-IV) from a related Chinese black earth tiger tarantula *Haplopelma hainanum* shares close sequence similarity to HwTx-IV (80% identical) and also retains the "^{26}RKxRWCK^{32}" motif in Loop 4 and C-terminus identical to HwTx-IV (Klint et al., 2012). HnTx-IV inhibits $Na_V1.7$ with IC_{50} of 21–34 nM (Cai et al., 2015; Li et al., 2004), similar to that of HwTx-IV, and mutations of positive charge residues K27A and R29A greatly diminished the affinity for $Na_V1.7$ (Li et al., 2004). On the $Na_V1.7$ side, mutations of E753Q, D816N, and E818Q similarly decreased HnTx-IV affinity by 2.0–130 fold (Cai et al., 2015). This indicates that both HwTx-IV and HnTx-IV share the same binding determinants to $Na_V1.7$ and likely bind to $Na_V1.7$ VS2 in a similar manner.

Author Manuscript Author Manuscript Author Manuscript Author Manuscript

ProTx-II is in NaSpTx family 3 and is much more distantly related to HwTx-IV (Figure S5A). Nevertheless, like HwTx-IV, it binds superficially to neurotoxin receptor site 4 in partially activated states of the VS and does not penetrate deeply into the aqueous cleft in VS2 (Figures S5B–S5D). The surface area of interaction with VS2 is <350 $Å^2$, similar to the low affinity interactions of HwTx-IV with a partially activated state of VS2 (Figure 5). Multiple complexes of ProTx-II with partially activated VS2 have been studied by cryo-EM (Shen et al., 2019; Xu et al., 2019). Although the VS in the structure of Xu et al. were proposed to represent deactivated states, their conformation is consistent with a partially activated intermediate state, as the S4 segment is located substantially outward from its position in the resting (ie., deactivated) state that we report here (Figures S5B–S5D). The structures of VS2 in these complexes form a series of partially activated intermediate states and activated states (Figure S6). The conformations of the voltage sensor in this series fit closely with the predictions of the sliding-helix model of voltage sensing (Catterall, 1986; Catterall et al., 2017; Yarov-Yarovoy et al., 2012). These structures suggest that ProTx-II can form low-affinity complexes with partially activated VS2 in multiple states. However, as we show here for HwTx-IV, it likely requires the resting state to form the high-affinity interactions involving a large surface area of the toxin and its receptor site, which are necessary for effective voltage-sensor trapping.

Implications for human $Na_V1.7$

Neurotoxin site 4 ligands like HwTx-IV and ProTx-II inhibit $Na_V1.7$ by trapping VS2 in the resting state, thereby preventing channel activation until a more positive membrane potential is reached. Our $Na_VAb/Na_V1.7$ VS2A chimera provides a structural basis for resting state trapping by HwTx-IV action. However, due to the tetrameric nature of the chimera, all voltage sensors are trapped in the resting state in a homogeneous fashion. This arrangement contrasts with eukaryotic sodium channels, which contain four homologous, but nonidentical, domains in a single polypeptide. HwTx-IV targets only VS2 in eukaryotic sodium channels (Xiao et al., 2014). Based on our results, we propose a mechanism for $Na_V1.7$ inhibition by HwTx-IV as follows. First, HwTx-IV approaches $Na_V1.7$ embedded in the plasma membrane at a negative resting membrane potential and binds tightly to the S1-S2 and S3-S4 helical hairpins and the aqueous cleft on VS2 in the resting state. Next, when the membrane potential is depolarized, the S4 helices in VS1, 3, and 4 move outward, priming the channel for opening. However, since VS2 is trapped in the resting state, the DII S4-S5 linker blocks S6 from moving, incapacitating pore opening. As long as HwTx-IV stays bound on VS2, the channel remains closed at physiologically accessible membrane potentials, and the action potential cannot be initiated or propagated.

Design and potential therapeutic significance of resting-state inhibitors of $Na_V1.7$

The mechanism for voltage-sensor trapping of $Na_V1.7$ in the resting state by gating-modifier toxins has significant implications for physiology and medicine. $Na_V1.7$ plays a key role in transmission of nociceptive information from the periphery to the spinal cord (Dib-Hajj et al., 2013). Gain-of-function mutations cause hyperalgesic syndromes, whereas loss-of-function mutations cause congenital indifference to pain (Dib-Hajj et al., 2013). Chronic pain is an unmet medical need that causes much loss of human potential and has driven the epidemic of opiate abuse. Drug discovery efforts have focused on sodium channel inhibitors

Author Manuscript Author Manuscript Author Manuscript Author Manuscript

that target activated states (Ahuja et al., 2015; Jarvis et al., 2007), but these compounds have not yet been successful in clinical use. Even in nociceptive afferents that are firing action potentials at maximal frequency, $Na_V1.7$ channels spend more than 90% of the time in the resting state between action potentials. Drugs that lock $Na_V1.7$ in the resting state would be powerful analgesics. Our results show that the resting state has a unique structure that can be in principle be effectively targeted by structure-based drug design, just as evolution has targeted this state-dependent structure by high-affinity neurotoxins. The binding surface we have revealed (Figure 6) is an excellent target for structure-based drug design, as it has a rigid array of positive, negative, and hydrophobic residues to mediate specific, high-affinity drug binding. We hope that our resting-state structure may provide guidance for future drug discovery efforts in targeting the resting state of sodium channels.

Limitations

Our conclusions are limited by the resolution of our cryo-EM structures. The resolution of the majority of the $Na_VAb/Na_V1.7$ chimera in its resting state is 3.5–4.0 Å (Figure 3). The resolution of m3-HwTx-IV is ~4.0 Å at the interface of m3-HwTx-IV with VS2A but declines to nearly 5 Å on the backside of the toxin away from the interface (Figure 3). In fitting the toxin into our cryo-EM density, we overcame these limitations by using the known NMR structure of m3-HwTx-IV, which is rigidly fixed by three disulfide bonds. The key amino acid side chains of the m3-HwTx-IV toxin and its target site on VS2A are well fit by the local cryo-EM density, as illustrated in Figures 5 and S3, which allowed us to build an accurate molecular model of the toxin/receptor interaction.

STAR METHODS

RESOURCE AVAILABILITY

Lead contact—Further information and requests for resources and reagents should be directed to and will be fulfilled by the Lead Contact, William A. Catterall (wcatt@uw.edu).

Materials Availability—Reagents generated in this study will be made available on request, but we may require a payment and/or a completed Materials Transfer Agreement if there is potential for commercial application.

Data and Code Availability—Cryo-EM map has been deposited in the Electron Microscopy Data Bank (EMDB) under accession code EMD-22661. The coordinates of the atomic model have been deposited in the PDB under accession code 7K48.

EXPERIMENTAL MODEL AND SUBJECT DETAILS

Microbe strains—*E. coli* GC10 was cultured at 37°C in LB medium supplemented with 100μg/ml of ampicillin for plasmid DNA extraction. *E. coli* DH10Bac was cultured at 37°C in LB medium supplemented with 50 μg/mL kanamycin sulfate, 7 μg/mL gentamicin and 10 μg/mL tetracycline for bacmid production.

Cell lines—Sf9 (*Spodoptera frugiperda*) insect cells were maintained in Grace's Insect Medium and supplemented with 10% FBS and penicillin/streptomycin at 27°C and passaged

Author Manuscript Author Manuscript Author Manuscript Author Manuscript

at 80–95% confluence for electrophysiology. Sf9 and Hi5 (*Trichoplusia ni*) insect cells were maintained and infected in Grace's Insect Medium supplemented with 7.5% FBS and glutamine/penicillin/streptomycin at 27°C for baculovirus production and protein expression, respectively.

METHOD DETAILS

Construction of $Na_VAb/Na_V1.7$-VS2 chimera—$Na_VAb/Na_V1.7$-VS2 cDNAs with a wide range of voltage-shifting mutations and combinations were constructed in order to explore the range of positive shifts in the voltage dependence of activation that are possible. These $Na_VAb/Na_V1.7$-VS2 chimeras were generated by grafting nucleotide sequences of S1-S2 and S3-S4 segments of $Na_V1.7$ VS2 into homologous regions in NaVAb. The cDNA encoding an initial chimera was gene synthesized, amplified by PCR, cloned into the pIZT vector, and modified by site-directed mutagenesis to generate different various chimera constructs that were then characterized by electrophysiology in Sf9 cells as described previously (Wisedchaisri et al., 2019). For more experimental details on construction and functional characterization of these constructs, see McCord, E., Broadband tuning the voltage dependence of a sodium channel. PhD Dissertation, University of Washington: https://digital.lib.washington.edu/researchworks/handle/1773/45249. The most positively shifted chimera ($Na_VAb/Na_V1.7$-VS2A), which contains the L834A mutation (equivalent to Na_VAb L109A (Wisedchaisri et al., 2019)), was selected for structural and functional studies with m3-HwTx-IV (Figures 1 and S1A).

DNA fragments of $Na_VAb/Na_V1.7$-VS2A were amplified by PCR from the pIZT $Na_VAb/Na_V1.7$-VS2A plasmid and fused to DNA fragments encoding maltose-binding protein (MBP) by overlap extension PCR (Heckman and Pease, 2007) to generate a gene encoding an N-terminal fusion of MBP-$Na_VAb/Na_V1.7$-VS2A with a rigid Asn-Ala linker and cloned into pFastBac Dual vector as described (Wisedchaisri et al., 2019). Baculoviruses containing the chimera were prepared using the Bac-to-Bac protocol according to the manufacturer with Sf9 insect cells (Life Technologies).

Electrophysiology—For initial characterization of cDNAs encoding $Na_V1.7/Na_VAb$-VS2 chimeras (Figures 1D and 1E), Sf9 insect cells (*Spodoptera frugiperda*) were transiently transfected with $Na_VAb/Na_V1.7$-VS2 containing the mutations indicated. Glass pipettes 1.5–3 MΩ were used to patch-clamp fluorescent cells, and currents were recorded via whole-cell voltage clamp (EPC10, Pulse, HEKA), sampled at 250 kHz, and filtered at 3 kHz. Membrane capacitance ranged from 5–25 pF. Rs was below 10 MΩ, with a 2 μs lag and at least 70% compensation, and voltage error was below 10 mV. A P/4 leak subtraction protocol was used. Standard recording solutions were as follows: Intracellular (in mM), NaCl (35), CsF (105), EGTA (10), HEPES (10), pH 7.4 (CsOH); Extracellular (in mM), NaCl (140), $MgCl_2$ (2), $CaCl_2$ (2) HEPES (10), pH 7.4 adjusted with NaOH ($[Na]_{Out}$ = 146 mM). As the G/V curves for the chimeras run through the reversal potential of sodium for these solutions (35 mV), these recordings were verified in solutions where NMDG-Cl (pH 7.0; HCl) was substituted for NaCl to move the reversal potential of sodium to 0 mV (35 NaCl/35 NaCl) and 100 mV (2.8 NaCl/140 NaCl). The pH for both intracellular and extracellular solutions was adjusted with $NMDG^+$ for these solutions. Osmolarity was

Author Manuscript Author Manuscript Author Manuscript Author Manuscript

adjusted with sucrose to match that of the cell growth media each day. Pulse data was analyzed using IGOR Pro (6.37).

For detailed voltage clamp studies of $Na_VAb/Na_V1.7$-VS2 chimeras (Figure 2), Hi5 insect cells (*Trichoplusia ni*) were infected with Baculovirus containing the chimera MBP-$Na_VAb/Na_V1.7$-VS2A. After 24–48h, whole-cell sodium currents were recorded using an Axopatch 200 amplifier (Molecular Devices) with glass micropipettes (1.5–3 MΩ). Capacitance was subtracted and 80–90% of series resistance was compensated using internal amplifier circuitry. I/V relationships of tail currents were recorded in response to steps to voltages ranging from −160 mV to 160 mV in 10-mV increments from a holding potential of −160 mV. Pulses were generated and currents were recorded using Pulse software controlling an Instrutech ITC18 interface (HEKA). Data were analysed using Igor Pro 8 (WaveMetrics). Sample sizes were chosen to give standard error of the mean (SEM) values of less than 10% of peak values based on prior experimental experience. Synthetic C-terminally amidated m3-HwTx-IV (>98% purity) was purchased from Alomone Laboratories.

Protein expression and purification—Third passage (P3) baculoviruses for MBP-$Na_VAb/Na_V1.7$-VS2A chimera were used to infect Hi5 cells in single-layer culture dishes, and the cells were incubated at 27°C for ~72 h. Cells were harvested by centrifugation. Cell pellets from ~20 dishes were resuspended in Buffer A (50 mM TrisHCl pH 7.5 and 200 mM NaCl) supplemented with 1 mM PMSF, 2X SigmaFast protease inhibitor cocktails, benzamidine HCl, and DNase I. Cells were lysed by sonication and membranes were solubilized with 1% high purity digitonin (Calbiochem) for 1 h at 4°C with gentle mixing. The mixture was centrifuged at 15,000×g for 30 min at 4°C, and the supernatant was incubated with amylose resin (NEB) for 1 h at 4°C with gentle mixing. The resins were washed with Buffer B (Buffer A supplemented with 0.06% w/v glycol-diosgenin (GDN; Anatrace)) and bound protein was eluted with Buffer C (Buffer B supplemented with 10 mM maltose). Eluted protein was concentrated to 1 ml using Vivaspin20 100kDa MWCO (Cytiva) and further purified with Superose 6 Increase size-exclusion chromatography (Cytiva) using 10 mM Tris HCl pH 7.5, 100 mM NaCl, and 0.006% GDN as a column running buffer. Elution fractions were evaluated using SDS-PAGE and peak fractions were combined and concentrated using Vivaspin6 100 kDa MWCO (Cytiva). m3-HwTx-IV was added to the chimera at 8:1 stoichiometric molar ratio of toxin to channel (8 molecules of toxin per 4 binding sites per channel), which corresponds to ~0.2–0.3 mM of m3-HwTx-IV to ~10 mg/ml of channel to ensure full binding occupancy. The mixture was incubated on ice for at least 30 min before grid preparation. Using this protocol, m3-huwentoxin-IV is co-eluted with MBP-$Na_VAb/Na_V1.7$-VS2A chimera on Superose 6 size-exclusion column (Figure S2A).

Cryo-EM sample preparation and data acquisition—Cryo-EM grids were prepared by applying m3-HwTx-IV: MBP-$Na_VAb/Na_V1.7$-VS2A complex in GDN detergent to glow-discharged holey carbon grids (Quantifoil Au R1.2/1.3, Quantifoil Micro Tools GmbH, Germany). Grids were blotted for 2.5 to 4.0 s using Vitrobot Mark IV (Thermo Fisher Scientific) and immediately plunge-frozen in liquid ethane cooled by liquid nitrogen. Cryo-

Author Manuscript Author Manuscript Author Manuscript Author Manuscript

EM data were recorded on a Titan Krios microscope (Thermo Fisher Scientific) operated at 300 kV, equipped with a GIF-quantum energy filter (Gatan) at 20 eV slit width and a K2 Summit direct detector (Gatan). LEGINON (Suloway et al., 2005) was used for automated data collection. Movies were collected at a nominal magnification of 130,000x in super-resolution mode resulting in a pixel size of 0.528 Å, with a small defocus range of −0.5 to −2.5 μm. The dose rate on the camera was set to be ~8 counts per physical pixel per second. The total exposure time was 8.6 s (0.2 s/frame), leading to a total accumulated dose of 60 electrons per $Å^2$ on the specimen (Table S1).

Cryo-EM image processing—Movie frames were aligned and 2x binned to a pixel size of 1.056 Å using MotionCor2 (Zheng et al., 2017), and the contrast transfer function parameters for each motion-corrected image were estimated using Gctf (Zhang, 2016). Subsequent image-processing steps were performed using RELION (Scheres, 2012) on an NVIDIA GPU-accelerated workstation. Particles were auto-picked using templates derived from 2D class averages that were initially generated from manually picked particles from ~50 images. A total of ~1.47 million particles from 7,168 good images were extracted into 256 × 256-pixel boxes and subjected to several rounds of 2D classification to remove bad particles (Figure S2C). 3D classification and refinement were carried out in RELION from 849,942 particles after 2D classification using the cryo-EM structure of Na_VAb that had been low-pass filtered to 60 Å as an initial model. The resulting 3D reconstructions were routinely better than 4.5 Å resolution. Subsequently, ~500k particles from a homogeneous class after RELION 3D classification and refinement were subjected to cycles of global and local refinement in cisTEM (Grant et al., 2018) using a reconstruction from RELION as a starting reference with the resolution limit set to 7.5 Å for particle alignment, and using a 3D mask that included the transmembrane and toxin regions while low-pass filtered the region outside (e.g. MBP, Na_VAb C-terminal tail, and detergent micelles) to 20 Å. The resolution was estimated using the Fourier shell correlation (FSC) between independently refined half-maps with a criterion value of 0.143 (Henderson et al., 2012) to be 3.6 Å (Figure S2D). Local resolution was evaluated using ResMap with two half maps as inputs (Kucukelbir et al., 2014) (Figure 3A).

Model building and refinement—Crystal structure of $Na_VAb/Na_V1.7$-VS2 with ProTx-II bound in the activated state (PDB 6N4I) was cleaned up to remove ProTx-II and small molecule ligands from the coordinates and subsequently docked into cryo-EM density map using Chimera (Pettersen et al., 2004). The atomic model was then rebuilt and locally refined using Coot (Emsley et al., 2010). NMR structure of m3-HwTx-IV (PDB 5T3M) (Rahnama et al. 2017) was docked into density for toxin on each voltage sensor initially by manual fitting, followed by rigid body fitting in Coot. The atomic model was subsequently refined using real space refinement in Phenix (Adams et al., 2010) with secondary structure restraints, noncrystallographic symmetry restraints, and reference model restraints of both main chains and side chains from the NMR structure of m3-HwTx-IV (Figure S3D and Table S1).

Structural analysis—Molecular contacts with distances within 5 Å were analyzed using program Contact in CCP4 Interface program suite (Potterton et al., 2003). Protein interfaces

Author Manuscript Author Manuscript Author Manuscript Author Manuscript

were analyzed using the program PISA (Krissinel and Henrick, 2007). Structure figures were made with Pymol (Schrodinger) and UCSF Chimera (Pettersen et al., 2004).

QUANTIFICATION AND STATISTICAL ANALYSIS

Analysis of electrophysiological data—Peak current at each voltage was averaged and plotted as a function of the stimulus voltage to yield a current vs. voltage (I/V) relationship. When the I/V curves contained only outward current, the reversal potential (V_{rev}) was verified with a separate protocol measuring the tail currents at peak activation. The instantaneous current of the tail current family was plotted as a function of voltage, fit with a line near 0 mV, and the X-intercept was used as V_{rev} to generate the conductance vs. voltage (G/V) curve from the I/V curve by calculating $G=I/(V_m-V_{rev})$. Normalized G/V curves were fit with a simple two-state Boltzmann equation, $1/(1+\exp(V_{1/2}-V_m)/k)$, in which V_m is the stimulus potential, $V_{1/2}$ is the half-activation voltage, and k is a slope factor. I/V plots of inward currents were fit with $(V_m-V_{rev})*(I_{min}/(1+\exp((V_m-V_{1/2})/k))$ to generate the Boltzmann curve fit to normalized G/V. Points within 10 mV of the reversal potential were omitted for the fit.

Estimation—Protein concentrations were estimated using an A280 extinction coefficient of 33,920 M^{-1} cm^{-1} on a spectrophotometer.

Global resolution estimation of cryo-EM density map is based on the 0.143 Fourier Shell Correlation criterion.

Supplementary Material

Refer to Web version on PubMed Central for supplementary material.

ACKNOWLEDGEMENTS

We thank Joel D. Quispe and Quinton Beedle (University of Washington Cryo-EM Facility) for technical assistance on cryo-EM, and Dr. Jin Li (Department of Pharmacology, University of Washington) for technical and editorial support. This research was supported by National Institutes of Health research grants R01 NS015751 (W.A.C.), R35 NS111573 (W.A.C.), and R01 HL112808 (W.A.C. and N.Z.), research training grant T32 GM007750 (E.M.), and by the Howard Hughes Medical Institute (N.Z.).

REFERENCES

Adams PD, Afonine PV, Bunkoczi G, Chen VB, Davis IW, Echols N, Headd JJ, Hung LW, Kapral GJ, Grosse-Kunstleve RW, et al. (2010). PHENIX: a comprehensive Python-based system for macromolecular structure solution. Acta Crystallogr D Biol Crystallogr 66, 213–221. [PubMed: 20124702]

Ahern CA, Payandeh J, Bosmans F, and Chanda B (2016). The hitchhiker's guide to the voltage-gated sodium channel galaxy. J Gen Physiol 147, 1–24. [PubMed: 26712848]

Ahuja S, Mukund S, Deng L, Khakh K, Chang E, Ho H, Shriver S, Young C, Lin S, Johnson JP Jr., et al. (2015). Structural basis of Nav1.7 inhibition by an isoform-selective small-molecule antagonist. Science 350, aac5464. [PubMed: 26680203]

Bezanilla F (2000). The voltage sensor in voltage-dependent ion channels. Physiol Rev 80, 555–592. [PubMed: 10747201]

Author Manuscript Author Manuscript Author Manuscript Author Manuscript

Cai T, Luo J, Meng E, Ding J, Liang S, Wang S, and Liu Z (2015). Mapping the interaction site for the tarantula toxin hainantoxin-IV (beta-TRTX-Hn2a) in the voltage sensor module of domain II of voltage-gated sodium channels. Peptides 68, 148–156. [PubMed: 25218973]

Catterall WA (1980). Neurotoxins that act on voltage-sensitive sodium channels in excitable membranes. AnnuRevPharmacolToxicol 20, 15–43.

Catterall WA (1984). The molecular basis of neuronal excitability. Science 223, 653–661. [PubMed: 6320365]

Catterall WA (1986). Molecular properties of voltage-sensitive sodium channels. AnnuRevBiochem 55, 953–985.

Catterall WA, Cestele S, Yarov-Yarovoy V, Yu FH, Konoki K, and Scheuer T (2007). Voltage-gated ion channels and gating modifier toxins. Toxicon 49, 124–141. [PubMed: 17239913]

Catterall WA, Wisedchaisri G, and Zheng N (2017). The chemical basis for electrical signaling. Nature Chem Biol 13, 455–463. [PubMed: 28406893]

Cestèle S, Qu Y, Rogers JC, Rochat H, Scheuer T, and Catterall WA (1998). Voltage sensor-trapping: Enhanced activation of sodium channels by beta-scorpion toxin bound to the S3-S4 loop in domain II. Neuron 21, 919–931. [PubMed: 9808476]

Couraud F, Jover E, Dubois JM, and Rochat H (1982). Two types of scorpion toxin receptor sites, one related to the activation, the other to the activation of the action potential sodium channel. Toxicon 20, 9–16. [PubMed: 6281941]

Dang S, van Goor MK, Asarnow D, Wang Y, Julius D, Cheng Y, and van der Wijst J (2019). Structural insight into TRPV5 channel function and modulation. Proc Natl Acad Sci U S A 116, 8869–8878. [PubMed: 30975749]

Dib-Hajj SD, Yang Y, Black JA, and Waxman SG (2013). The NaV1.7 sodium channel: from molecule to man. Nat Rev Neurosci 14, 49–62. [PubMed: 23232607]

Emsley P, Lohkamp B, Scott WG, and Cowtan K (2010). Features and development of Coot. Acta Crystallogr D Biol Crystallogr 66, 486–501. [PubMed: 20383002]

Gamal El-Din TM, Lenaeus MJ, and Catterall WA (2018). Structural and functional analysis of sodium channels viewed from an evolutionary perspective. Handb Exp Pharmacol 246, 53–72. [PubMed: 29043505]

Gamal El-Din TM, Martinez GQ, Payandeh J, Scheuer T, and Catterall WA (2013). A gating charge interaction required for late slow inactivation of the bacterial sodium channel Na_VAb. J Gen Physiol 142, 181–190. [PubMed: 23980192]

Gao S, Valinsky WC, On NC, Houlihan PR, Qu Q, Liu L, Pan X, Clapham DE, and Yan N (2020). Employing NaChBac for cryo-EM analysis of toxin action on voltage-gated Na(+) channels in nanodisc. Proc Natl Acad Sci U S A 117, 14187–14193. [PubMed: 32513729]

Grant T, Rohou A, and Grigorieff N (2018). cisTEM, user-friendly software for single-particle image processing. Elife 7.

Heckman KL, and Pease LR (2007). Gene splicing and mutagenesis by PCR-driven overlap extension. Nat Protoc 2, 924–932. [PubMed: 17446874]

Henderson R, Sali A, Baker ML, Carragher B, Devkota B, Downing KH, Egelman EH, Feng Z, Frank J, Grigorieff N, et al. (2012). Outcome of the first electron microscopy validation task force meeting. Structure 20, 205–214. [PubMed: 22325770]

Hille B (1975). The receptor for tetrodotoxin and saxitoxin: a structural hypothesis. BiophysJ 15, 615–619. [PubMed: 1148362]

Hille B (2001). Ionic Channels of Excitable Membranes, 3rd Ed (Sunderland, MA: Sinauer Associates Inc.).

Hodgkin AL, and Huxley AF (1952). A quantitative description of membrane current and its application to conduction and excitation in nerve. JPhysiol 117, 500–544. [PubMed: 12991237]

Jarvis MF, Honore P, Shieh CC, Chapman M, Joshi S, Zhang XF, Kort M, Carroll W, Marron B, Atkinson R, et al. (2007). A-803467, a potent and selective Nav1.8 sodium channel blocker, attenuates neuropathic and inflammatory pain in the rat. Proc Natl Acad Sci U S A 104, 8520–8525. [PubMed: 17483457]

Author Manuscript Author Manuscript Author Manuscript Author Manuscript

Jiang D, Shi H, Tonggu L, Gamal El-Din TM, Lenaeus MJ, Zhao Y, Yoshioka C, Zheng N, and Catterall WA (2020). Structure of the cardiac sodium channel. Cell 180, 122–134. [PubMed: 31866066]

Klint JK, Senff S, Rupasinghe DB, Er SY, Herzig V, Nicholson GM, and King GF (2012). Spider-venom peptides that target voltage-gated sodium channels: pharmacological tools and potential therapeutic leads. Toxicon 60, 478–491. [PubMed: 22543187]

Krissinel E, and Henrick K (2007). Inference of macromolecular assemblies from crystalline state. J Mol Biol 372, 774–797. [PubMed: 17681537]

Kucukelbir A, Sigworth FJ, and Tagare HD (2014). Quantifying the local resolution of cryo-EM density maps. Nat Methods 11, 63–65. [PubMed: 24213166]

Lazdunski M, Frelin C, Barhanin J, Lombet A, Meiri H, Pauron D, Romey G, Schmid A, Schweitz H, Vigne P, et al. (1986). Polypeptide toxins as tools to study voltage-sensitive Na+ channels. Ann N Y Acad Sci 479, 204–220. [PubMed: 2433992]

Li D, Xiao Y, Xu X, Xiong X, Lu S, Liu Z, Zhu Q, Wang M, Gu X, and Liang S (2004). Structure--activity relationships of hainantoxin-IV and structure determination of active and inactive sodium channel blockers. J Biol Chem 279, 37734–37740. [PubMed: 15201273]

Middleton RE, Warren VA, Kraus RL, Hwang JC, Liu CJ, Dai G, Brochu RM, Kohler MG, Gao YD, Garsky VM, et al. (2002). Two tarantula peptides inhibit activation of multiple sodium channels. Biochemistry 41, 14734–14747. [PubMed: 12475222]

Numa S, and Noda M (1986). Molecular structure of sodium channels. Ann N Y Acad Sci 479, 338–355. [PubMed: 2434000]

Pan X, Li Z, Huang X, Huang G, Gao S, Shen H, Liu L, Lei J, and Yan N (2019). Molecular basis for pore blockade of human Na^+ channel $Na_V1.2$ by the mu-conotoxin KIIIA. Science 363, 1309–1313. [PubMed: 30765605]

Pan X, Li Z, Zhou Q, Shen H, Wu K, Huang X, Chen J, Zhang J, Zhu X, Lei J, et al. (2018). Structure of the human voltage-gated sodium channel $Na_V1.4$ in complex with beta1. Science 362, pii: eaau2486.

Payandeh J, Gamal El-Din TM, Scheuer T, Zheng N, and Catterall WA (2012). Crystal structure of a voltage-gated sodium channel in two potentially inactivated states. Nature 486 135–139. [PubMed: 22678296]

Payandeh J, Scheuer T, Zheng N, and Catterall WA (2011). The crystal structure of a voltage-gated sodium channel. Nature 475, 353–358. [PubMed: 21743477]

Peng K, Shu Q, Liu Z, and Liang S (2002). Function and solution structure of huwentoxin-IV, a potent neuronal tetrodotoxin (TTX)-sensitive sodium channel antagonist from Chinese bird spider Selenocosmia huwena. J Biol Chem 277, 47564–47571. [PubMed: 12228241]

Pettersen EF, Goddard TD, Huang CC, Couch GS, Greenblatt DM, Meng EC, and Ferrin TE (2004). UCSF Chimera--a visualization system for exploratory research and analysis. J Comput Chem 25, 1605–1612. [PubMed: 15264254]

Potterton E, Briggs P, Turkenburg M, and Dodson E (2003). A graphical user interface to the CCP4 program suite. Acta Crystallogr D Biol Crystallogr 59, 1131–1137. [PubMed: 12832755]

Rahnama S, Deuis JR, Cardoso FC, Ramanujam V, Lewis RJ, Rash LD, King GF, Vetter I, and Mobli M (2017). The structure, dynamics and selectivity profile of a NaV1.7 potency-optimised huwentoxin-IV variant. PLoS One 12, e0173551. [PubMed: 28301520]

Rajamani R, Wu S, Rodrigo I, Gao M, Low S, Megson L, Wensel D, Pieschl RL, Post-Munson DJ, Watson J, et al. (2017). A Functional NaV1.7-NaVAb Chimera with a Reconstituted High-Affinity ProTx-II Binding Site. Mol Pharmacol 92, 310–317. [PubMed: 28645932]

Ren D, Navarro B, Xu H, Yue L, Shi Q, and Clapham DE (2001). A prokaryotic voltage-gated sodium channel. Science 294, 2372–2375. [PubMed: 11743207]

Revell JD, Lund PE, Linley JE, Metcalfe J, Burmeister N, Sridharan S, Jones C, Jermutus L, and Bednarek MA (2013). Potency optimization of Huwentoxin-IV on hNav1.7: a neurotoxin TTX-S sodium-channel antagonist from the venom of the Chinese bird-eating spider Selenocosmia huwena. Peptides 44, 40–46. [PubMed: 23523779]

Ritchie JM (1979). A pharmacological approach to the structure of sodium channels in myelinated axons. Annu Rev Neurosci 2, 341–362. [PubMed: 395883]

Author Manuscript Author Manuscript Author Manuscript Author Manuscript

Rochat H, Bernard P, and Couraud F (1979). Scorpion toxins: chemistry and mode of action. Adv Cytopharmacol 3, 325–334. [PubMed: 382791]

Rogers JC, Qu Y, Tanada TN, Scheuer T, and Catterall WA (1996). Molecular determinants of high affinity binding of alpha-scorpion toxin and sea anemone toxin in the S3-S4 extracellular loop in domain IV of the Na^+ channel alpha subunit. JBiolChem 271, 15950–15962.

Scheres SH (2012). RELION: implementation of a Bayesian approach to cryo-EM structure determination. J Struct Biol 180, 519–530. [PubMed: 23000701]

Schmalhofer WA, Calhoun J, Burrows R, Bailey T, Kohler MG, Weinglass AB, Kaczorowski GJ, Garcia ML, Koltzenburg M, and Priest BT (2008). ProTx-II, a selective inhibitor of NaV1.7 sodium channels, blocks action potential propagation in nociceptors. Mol Pharmacol 74, 1476–1484. [PubMed: 18728100]

Shaya D, Findeisen F, Abderemane-Ali F, Arrigoni C, Wong S, Nurva SR, Loussouarn G, and Minor DL Jr. (2014). Structure of a prokaryotic sodium channel pore reveals essential gating elements and an outer ion binding site common to eukaryotic channels. J Mol Biol 426, 467–483. [PubMed: 24120938]

Shen H, Liu D, Wu K, Lei J, and Yan N (2019). Structures of human $Na_V1.7$ channel in complex with auxiliary subunits and animal toxins. Science 363, 1303–1308. [PubMed: 30765606]

Singh AK, McGoldrick LL, Twomey EC, and Sobolevsky AI (2018). Mechanism of calmodulin inactivation of the calcium-selective TRP channel TRPV6. Sci Adv 4, eaau6088. [PubMed: 30116787]

Sokolov S, Kraus RL, Scheuer T, and Catterall WA (2008). Inhibition of sodium channel gating by trapping the domain II voltage sensor with protoxin II. Mol Pharmacol 73, 1020–1028. [PubMed: 18156314]

Sula A, Booker J, Ng LC, Naylor CE, DeCaen PG, and Wallace BA (2017). The complete structure of an activated open sodium channel. Nat Commun 8, 14205. [PubMed: 28205548]

Suloway C, Pulokas J, Fellmann D, Cheng A, Guerra F, Quispe J, Stagg S, Potter CS, and Carragher B (2005). Automated molecular microscopy: the new Leginon system. J Struct Biol 151, 41–60. [PubMed: 15890530]

Waugh DS (2016). Crystal structures of MBP fusion proteins. Protein Sci 25, 559–571. [PubMed: 26682969]

Wisedchaisri G, Tonggu L, McCord E, Gamal El-Din TM, Wang L, Zheng N, and Catterall WA (2019). Resting-state structure and gating mechanism of a voltage-gated sodium channel. Cell 178, 993–1003. [PubMed: 31353218]

Xiao Y, Bingham JP, Zhu W, Moczydlowski E, Liang S, and Cummins TR (2008a). Tarantula huwentoxin-IV inhibits neuronal sodium channels by binding to receptor site 4 and trapping the domain ii voltage sensor in the closed configuration. J Biol Chem 283, 27300–27313. [PubMed: 18628201]

Xiao Y, Blumenthal K, and Cummins TR (2014). Gating-pore currents demonstrate selective and specific modulation of individual sodium channel voltage-sensors by biological toxins. Mol Pharmacol 86, 159–167. [PubMed: 24898004]

Xiao Y, Blumenthal K, Jackson JO 2nd, Liang S, and Cummins TR (2010). The tarantula toxins ProTx-II and huwentoxin-IV differentially interact with human Nav1.7 voltage sensors to inhibit channel activation and inactivation. Mol Pharmacol 78, 1124–1134. [PubMed: 20855463]

Xiao Y, Jackson JO, 2nd, Liang S, and Cummins TR (2011). Common molecular determinants of tarantula huwentoxin-IV inhibition of Na+ channel voltage sensors in domains II and IV. J Biol Chem 286, 27301–27310. [PubMed: 21659528]

Xiao Y, Luo X, Kuang F, Deng M, Wang M, Zeng X, and Liang S (2008b). Synthesis and characterization of huwentoxin-IV, a neurotoxin inhibiting central neuronal sodium channels. Toxicon 51, 230–239. [PubMed: 18054060]

Xu H, Li T, Rohou A, Arthur CP, Tzakoniati F, Wong E, Estevez A, Kugel C, Franke Y, Chen J, et al. (2019). Structural basis of Nav1.7 inhibition by agating-modifier spider toxin. Cell.

Yarov-Yarovoy V, Decaen PG, Westenbroek RE, Pan CY, Scheuer T, Baker D, and Catterall WA (2012). Structural basis for gating charge movement in the voltage sensor of a sodium channel. Proc Natl Acad Sci USA 109 E93–E102. [PubMed: 22160714]

Author Manuscript Author Manuscript Author Manuscript Author Manuscript

Zhang JZ, Yarov-Yarovoy V, Scheuer T, Karbat I, Cohen L, Gordon D, Gurevitz M, and Catterall WA (2011). Structure-function map of the receptor site for beta-scorpion toxins in domain II of voltage-gated sodium channels. J Biol Chem 286, 33641–33651. [PubMed: 21795675]

Zhang JZ, Yarov-Yarovoy V, Scheuer T, Karbat I, Cohen L, Gordon D, Gurevitz M, and Catterall WA (2012a). Mapping the interaction site for a beta-scorpion toxin in the pore module of domain III of voltage-gated Na^+ channels. J Biol Chem 287, 30719–30728. [PubMed: 22761417]

Zhang K (2016). Gctf: Real-time CTF determination and correction. J Struct Biol 193, 1–12. [PubMed: 26592709]

Zhang X, Ren W, DeCaen P, Yan C, Tao X, Tang L, Wang J, Hasegawa K, Kumasaka T, He J, et al. (2012b). Crystal structure of an orthologue of the NaChBac voltage-gated sodium channel. Nature 486, 130–134. [PubMed: 22678295]

Zheng SQ, Palovcak E, Armache JP, Verba KA, Cheng Y, and Agard DA (2017). MotionCor2: anisotropic correction of beam-induced motion for improved cryo-electron microscopy. Nat Methods 14, 331–332. [PubMed: 28250466]

Author Manuscript Author Manuscript Author Manuscript Author Manuscript

Highlights

- Tarantula toxin and voltage-shifting mutations trap resting state of $Na_V1.7$ chimera
- The toxin forms a high-affinity complex with the S3-S4 linker of the voltage sensor
- Huwentoxin inserts a key lysine like a ‘stinger’ into a triad of negative charges
- The structure vividly illuminates the molecular mechanism of voltage-sensor trapping
- The results offer an initial molecular template for future design of analgesic drugs

Author Manuscript Author Manuscript Author Manuscript Author Manuscript

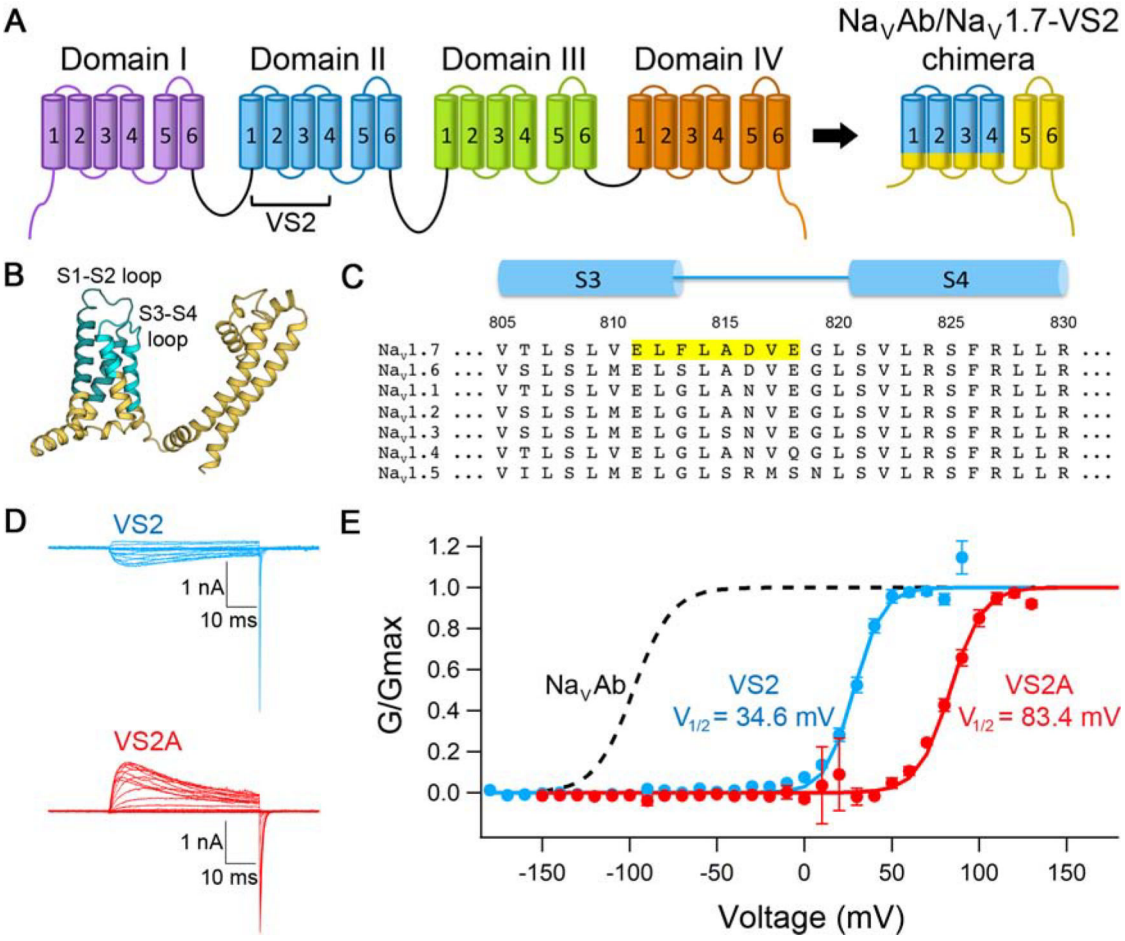

Figure 1. Design of Voltage Shifting $Na_VAb/Na_V1.7$-VS2 Chimera

(A) Topology diagram of substitution. Transmembrane and extracellular portion of human $Na_V1.7$ VS2 S1-S2 and S3-S4 helices (cyan) were grafted onto equivalent region of Na_VAb (gold).

(B) Model of substitution. Cyan highlights portions of human $Na_V1.7$ S1-S2 and S3-S4 helices that have been grafted onto Na_VAb (gold).

(C) Sequence alignment of S3-S4 region of different human Na_V subtypes. Sequence portion including the “LFLAD” motif that interacts with HwTx-IV is highlighted in yellow.

(D) Representative current families of $Na_VAb/Na_V1.7$-VS2 chimera (cyan) and with L834A mutation (VS2A) (red). Transiently transfected Sf9 cells were held at −150 mV and stimulated for 50 ms to depolarized voltages in 10 mV increments. Scale bars represent 10 msec × 1 nA.

(E) Normalized conductance-voltage (G/V) relationships and Boltzmann fits for Na_VAb (black dash; WT (Gamal El-Din et al., 2013)), $Na_VAb/Na_V1.7$-VS2 chimera alone (cyan; $V_{1/2}$ = 34.6 ± 1.4 mV, k = 10.0, n = 0.1, n = 6) and with L834A mutation (VS2A) (red; $V_{1/2}$ = 83.4 ± 0.9 mV, k=9.1 ± 0.6, n = 3). Markers and error bars represent average G/G_{max} ± standard error of the mean (SEM). Half activation ($V_{1/2}$) and slope (k) values are averages of individual fits ± SEM. Curves = $1/(1+ê((V_{1/2}-V_m)/k))$.

See also Figure S1.

Author Manuscript Author Manuscript Author Manuscript Author Manuscript

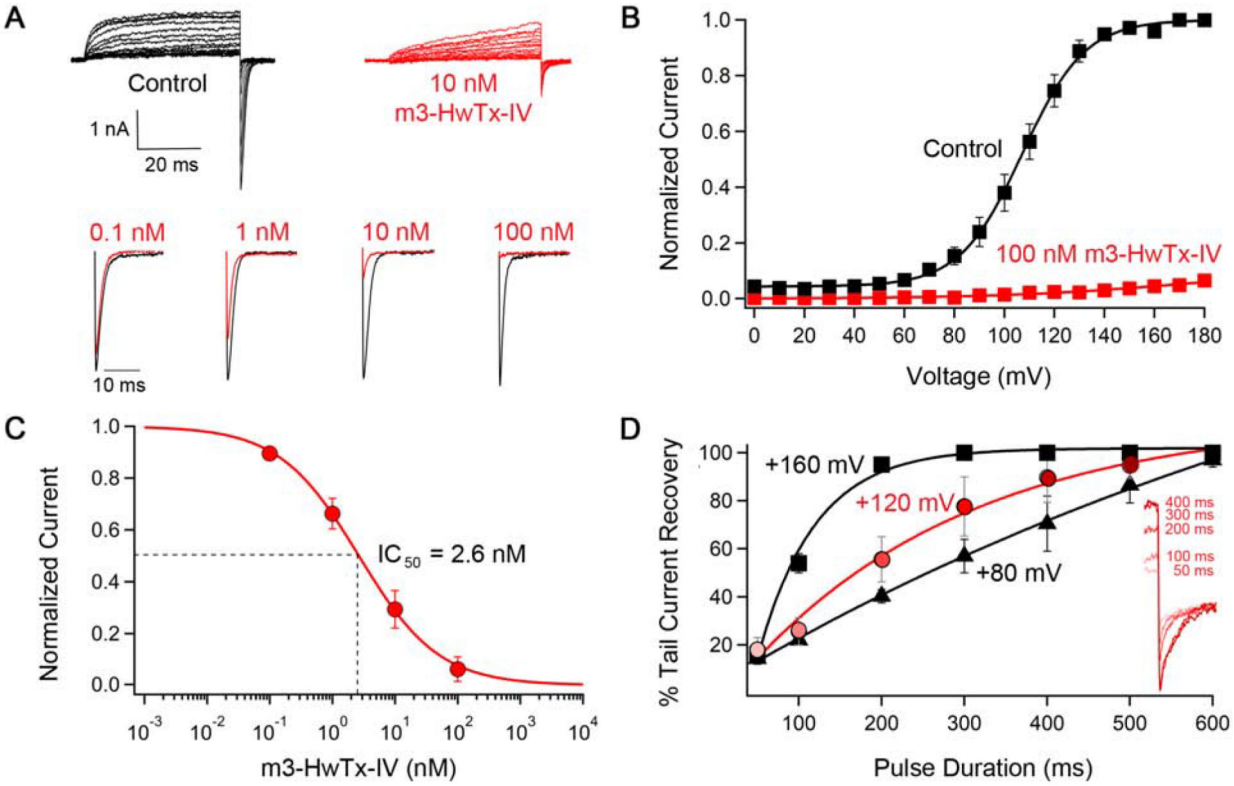

Figure 2. Voltage Sensor Trapping of $Na_VAb/Na_V1.7$ VS2A by m3-HwTx-IV.

(A) Representative traces of sodium outward currents and following inward tail currents in Hi5 cells in response to 50-ms pulses from a holding potential of −160 mV in 10 mV steps from 0 mV to +160 mV (Black). Sodium currents measured from the same cell after perfusion with 10 nM m3-HwTx-IV (Red). Tail currents before (black) and after (red) treatment with different concentrations of m3-HwTx-IV (0.1, 1, 10, and 100 nM as indicated).

(B) Normalized Current/Voltage (I/V) plot of $Na_VAb/Na_V1.7$-VS2A before (black) and after (red) treating cells with 100 nM m3-HwTx-IV. Tail currents measured after m3-HwTx-IV treatment were normalized to the one measured previously. Conductance was estimated from the tail current amplitude and normalized to the control amplitude at the +160-mV test potential. The solid black line is the fit of the Boltzmann equation to the data. The $V_{1/2}$ was 107.2 ± 0.5 mV with a slope factor K= 12.5 ± 0.3. Data are represented as mean ± SEM with n = 5 to 8.

(C) Concentration-response curve of m3-HwTx-IV interaction with $Na_VAb/Na_V1.7$-VS2A chimera. The solid red line is the best fit using the Hill equation. IC_{50}= 2.6 ± 0.3 nM with a Hill coefficient = 0.7. Data are represented as mean ± SEM with n = 5 to 7.

(D) Time course for recovery of blocked tail current following strong depolarizations in the presence of 250 nM m3-HwTx-IV. Current amplitude was measured at +80, +120, and +160 mV. Different pulse durations were used from 50-ms to 600-ms. Recovered currents were normalized to the peak current elicited from depolarizations to 600-ms. Data are represented as mean ± SEM with n = 3 to 5. *Inset.* Representative current traces of recovered currents at +120 mV depolarizing potentials.

Author Manuscript Author Manuscript Author Manuscript Author Manuscript

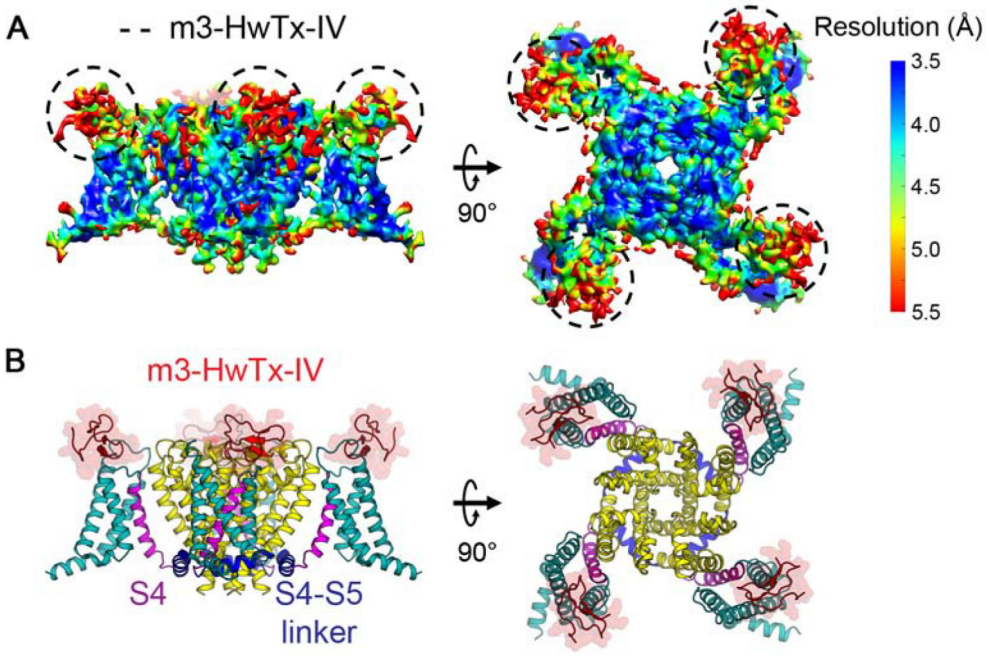

Figure 3. Cryo-EM Structure of $Na_VAb/Na_V1.7$ VS2A Chimera in the Resting State Trapped by m3-HwTx-IV.

(A) Cryo-EM density map colored by local resolution in side and top views. Local resolution was evaluated using ResMap (Kucukelbir et al., 2014). The right panel shows resolution spectrum bar.

(B) Overall structure of m3-HwTx-IV:$Na_VAb/Na_V1.7$-VS2A chimera. Side view (left) and top view (right) are shown in the same orientation as in (A). S0 to S3 segments of the VS are colored in teal and S4 in magenta. The S4-S5 linker is highlighted in blue and the pore module in yellow. m3-HwTx-IV is colored in red superimposed with transparent van der Waals surface.

See also Figures S2 and S3, and Table S1.

Author Manuscript Author Manuscript Author Manuscript Author Manuscript

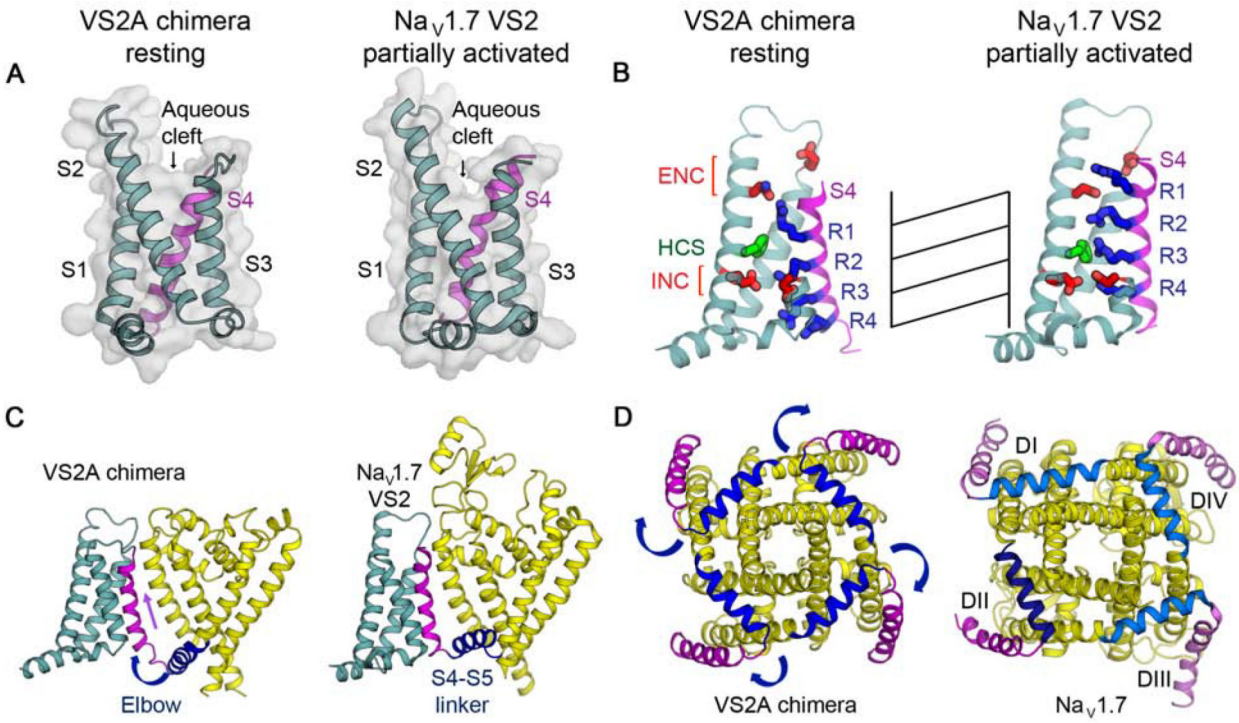

Figure 4. Structure of $Na_VAb/Na_V1.7$-VS2A Trapped by m3-HwTx-IV in the Resting State and Comparison to $Na_V1.7$ VS2 Trapped by HwTx-IV in a Partially Activated State.

(Left panels) $Na_VAb/Na_V1.7$-VS2A in the resting state; (Right panels) $Na_V1.7$ VS2 in a partially activated state bound to HwTx-IV + saxitoxin (PDB 6J8G)

(A) Structures of the VS as backbone cartoon superimposed with the molecular surface. S0 to S3 are shown in light teal and S4 in magenta. An aqueous cleft between S1-S2 and S3-S4 helix-loop-helix is indicated.

(B) Gating charge movement. Four Arg gating charges R1-R4 (blue), extracellular negative charge (ENC) cluster of E753 on S1 and N769 on S2, intracellular negative charge (INC) cluster of E779 on S2 and D801 on S3 (red), and F776 in the hydrophobic constriction site (HCS) (green) are shown in sticks. S4 (magenta) moves outward from resting state to partially activated state by ~7.3 Å, passing nearly two gating charges through the HCS on S2. Part of S3 is omitted for clarity.

(C) Side view of the structures with the S0 to S3 segments shown in gray, S4 in magenta, the S4-S5 linker in blue, and the pore module in yellow. The S4 segment moves outward across the membrane from the resting to the partially activated states while the S1 to S3 segments remain relatively unchanged with respect to the membrane. The S4-S5 linker acts as an elbow that connects the S4 movement to modulate the pore. Three VS and two pore modules are omitted for clarity.

(D) Bottom (intracellular) view of the structures in (C) with complete pore modules. The S4-S5 linker (blue) undergoes a large conformational change that tightens the collar around the S5 and S6 segments (yellow) of the pore in the resting state and loosens the collar in the partially activated state. S0 to S3 are omitted for clarity.

See also Figures S4 and S6.

Author Manuscript Author Manuscript Author Manuscript Author Manuscript

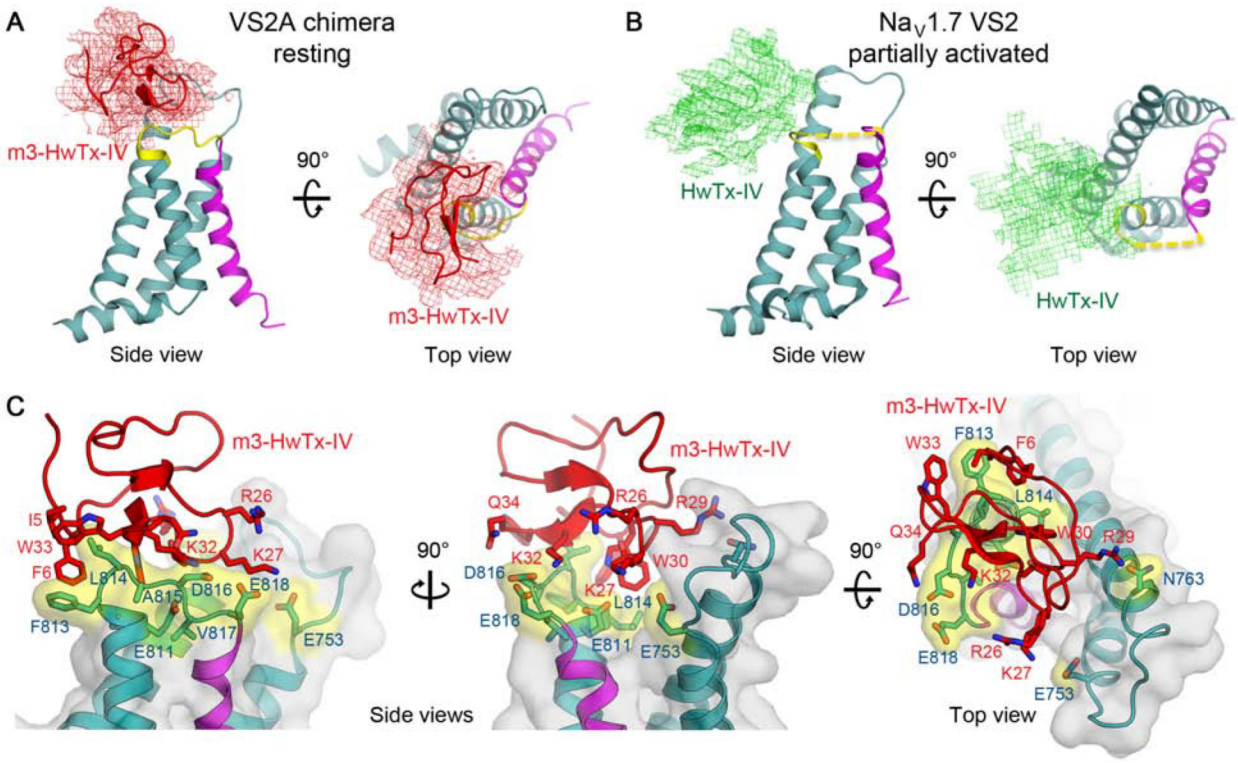

Figure 5. Molecular Interactions of HwTx-IV with Neurotoxin Receptor Site 4 in Resting and Partially Activated Na$_V$1.7-VS2

(A) Binding position of m3-HwTx-IV to the resting state of neurotoxin receptor site 4 of Na$_V$Ab/Na$_V$1.7-VS2A in side and top views. Cryo-EM density map filtered to 4.5 Å resolution for m3-HwTx-IV (red) is shown superimposed with the atomic model.

(B) Binding position of HwTx-IV to the partially activated state of neurotoxin receptor site 4 of Na$_V$1.7 in side and top views. Cryo-EM density map (EMD-9781) filtered to 4.5 Å resolution for HwTx-IV (green) is shown in comparison to (A).

(C) Detailed molecular interactions of m3-HwTx-IV with Na$_V$Ab/Na1.7-VS2A chimera in the resting state. Residues making contacts within 5 Å are shown as sticks models and highlighted in yellow for residues from VS2 chimera as in Figure 1C. Some parts of the interactions were only partially resolved in the experimentally determined density and were modeled based on rigid-body docking and refinement of the known NMR structure of the toxin.

See also Figure S5.

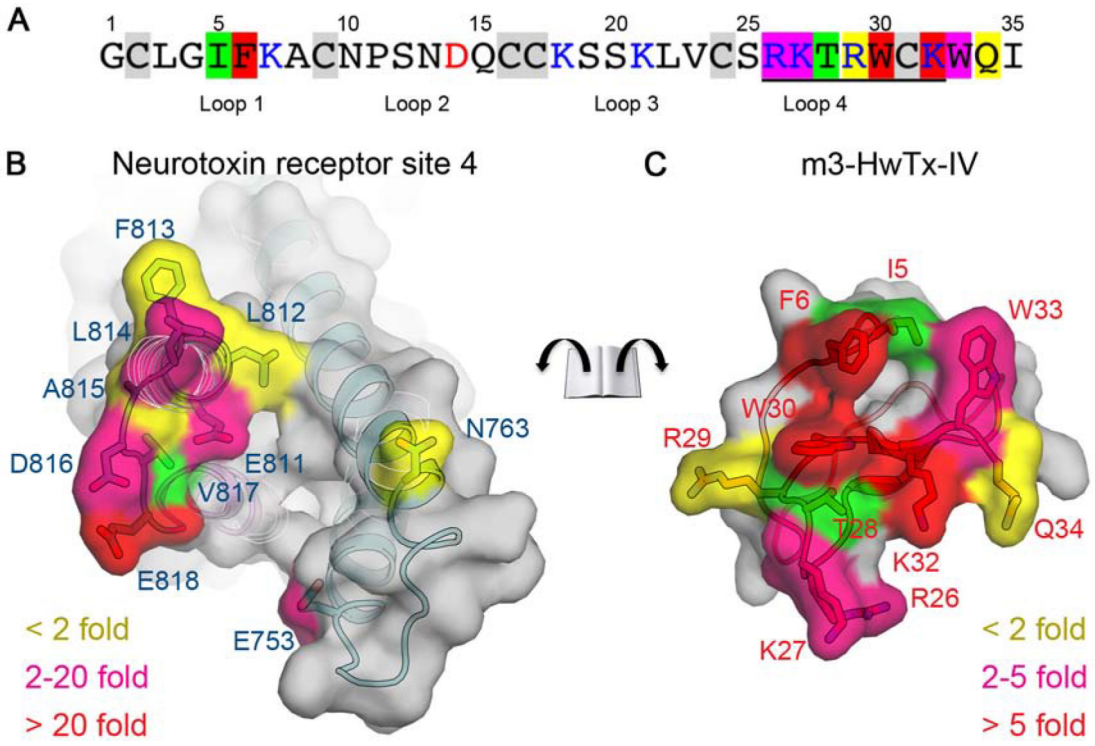

Figure 6. Detailed Map of Interactions Between m3-HwTx-IV and VS2

(A) Amino acid sequence of m3-HwTx-IV. Cysteine residues that form disulfide bonds are highlighted in gray. Positive charge and negative charge residues are colored in blue and red letters, respectively. Residues of m3-HwTx-IV that when mutated to alanine resulted in a loss of affinity for $Na_V1.7$ by less than 2-fold are highlighted in yellow, 2–5-fold are in pink, and more than 5-fold in red, or positive gain in affinity in green according to (Revell et al., 2013). The C-terminal "^{26}RKxRWCK^{32}" motif important for binding is underlined.

(B) Close up top view as in Figure 5C right panel with m3-HwTx-IV removed. Surface residues are colored based on changes in affinity when mutated according to (Xiao et al., 2011).

(C) Close up view as in Figure 5C right panel with m3-HwTx-IV turned 180° open face up to show resides making interactions with the Na_VAb/Na1.7-VS2A. Surface residues are colored based on changes in affinity when mutated to Ala as in (A).

Author Manuscript Author Manuscript Author Manuscript Author Manuscript

Author Manuscript Author Manuscript Author Manuscript Author Manuscript

KEY RESOURCES TABLE

REAGENT or RESOURCE	SOURCE	IDENTIFIER
Bacterial and Virus Strains		
E. coli BL21(DE3)	NEB	Cat# C2527I
E. coli DH10Bac	ThermoFisher Scientific	Cat# 10361-012
Chemicals, Peptides, and Recombinant Proteins		
Amylose resin	NEB	Cat# E8021S
Digitonin, High Purity	Millipore Sigma	Cat# 300410
Glycol-diosgenin (GDN)	Anatrace	Cat# GDN101
m3-huwentoxin-IV (m3-HWTX-IV)	Alamone Labs	Cat# STH-102
Deposited Data		
Coordinates of $Na_VAb/Na_V1.7$-VS2A: m3-HwTx-IV	This study	PDB: 7K48
Cryo-EM Map of $Na_VAb/Na_V1.7$-VS2A: m3-HwTx-IV	This study	EMDB: EMD-22661
Experimental Models: Cell Lines		
Spodoptera frugiperda (Sf9)	Life Technologies	B825-01
Trichoplusia ni (High Five)	Life Technologies	B855-02
Oligonucleotides		
EcoRI-MBP forward primer: CGCGCGGAATTCATGAAAATCGAAGAAGGTAAACTGG	Integrated DNA Technologies (IDT)	N/A
MBP-NA1-Na_VAb reverse primer: GTAATTGCAAGATACATAGCATTAGTCTGCGCGTCTTTCAGGGC	Integrated DNA Technologies (IDT)	N/A
MBP-NA1-Na_VAb forward primer: GCGCAGACTAATGCTATGTATCTTGCAATTACAAATATTGTAG	Integrated DNA Technologies (IDT)	N/A
Na_VAb-HindIII reverse primer: CGACAAGCTTTTATTAGTTTTTTAAACTAGTTTTTATTAATTCTTTAAG	Integrated DNA Technologies (IDT)	N/A
Recombinant DNA		
pFastBacDual MBP-$Na_VAb/Na_V1.7$-VS2A	This study	N/A
pIZT GFP-P2A-$Na_VAb/Na_V1.7$-VS2	This study	N/A
pIZT GFP-P2A-$Na_VAb/Na_V1.7$-VS2A	This study	N/A
Software and Algorithms		
CCP4i 7.0.068	CCP4	http://www.ccp4.ac.uk
Chimera 1.11.2	UCSF	https://www.cgl.ucsf.edu/chimera
CisTEM 1.0.0-beta	CisTEM	https://cistem.org
Coot 0.8.9.1	MRC	https://www2.mrc-lmb.cam.ac.uk/personal/pemsley/coot
Gctf	MRC	https://www.mrc-lmb.cam.ac.uk/kzhang
IGOR Pro 6.37	WaveMetrics	https://www.wavemetrics.com

Author Manuscript
Author Manuscript
Author Manuscript
Author Manuscript

REAGENT or RESOURCE	SOURCE	IDENTIFIER
Leginon 3.3	NRAMM	http://leginon.org
MotionCor2	UCSF	https://msg.ucsf.edu/software
Phenix 1.14-3260	Phenix consortium	https://www.phenix-online.org
Pymol 1.7.2	Schrödinger	https://pymol.org
Relion 3.0 beta	MRC	https://www2.mrc-lmb.cam.ac.uk/relion
ResMap	Kucukelbir et al., 2014	http://resmap.sourceforge.net/